The Astrophysical Journal, 665:1448–1459, 2007 August 20

WHAT DETERMINES THE INTENSITY OF SOLAR FLARE/CME EVENTS?

Yingna Su,[1,2] Adriaan Van Ballegooijen,[1] James McCaughey,[1]
Edward DeLuca,[1] Katharine K. Reeves,[1] and Leon Golub[1]
Received 2007 February 19; accepted 2007 May 8

ABSTRACT

We present a comprehensive statistical study addressing the question of what determines the intensity of a solar flare and associated coronal mass ejection (CME). For a sample of 18 two-ribbon flares associated with CMEs, we have examined the correlations between the *GOES* soft X-ray peak flare flux (PFF), the CME speed ($V_{\rm CME}$) obtained from *SOHO* LASCO observations, and six magnetic parameters of the flaring active region. These six parameters measured from both *TRACE* and *SOHO* MDI observations are: the average background magnetic field strength (B), the area of the region where B is counted (S), the magnetic flux of this region (Φ), the initial shear angle (θ_1, measured at the flare onset), the final shear angle (θ_2, measured at the time when the shear change stops), and the change of shear angle ($\theta_{12} = \theta_1 - \theta_2$) of the footpoints. We have found no correlation between θ_1 and the intensity of flare/CME events, while the other five parameters are either positively or negatively correlated with both $\log_{10}$(PFF) and $V_{\rm CME}$. Among these five parameters, Φ and θ_{12} show the most significant correlations with $\log_{10}$(PFF) and $V_{\rm CME}$. The fact that both $\log_{10}$(PFF) and $V_{\rm CME}$ are highly correlated with θ_{12} rather than with θ_1 indicates that the intensity of flare/CME events may depend on the *released* magnetic free energy rather than the *total* free energy stored prior to the flare. We have also found that a linear combination of a subset of these six parameters shows a much better correlation with the intensity of flare/CME events than each parameter itself, and the combination of $\log_{10}\Phi$, θ_1, and θ_{12} is the top-ranked combination.

Subject headings: Sun: corona — Sun: coronal mass ejections (CMEs) — Sun: flares — Sun: magnetic fields — Sun: photosphere

1. INTRODUCTION

Solar flares, prominence eruptions, and coronal mass ejections (CMEs) are magnetic phenomena thought to be powered by the magnetic free energy (i.e., the difference between the observed total magnetic energy and the potential field magnetic energy) stored in the corona prior to the eruption. Storage of free energy requires a nonpotential magnetic field, and it is therefore associated with a shear or twist in the coronal field away from the potential, current-free state (Priest & Forbes 2002). One indication of such a stressed magnetic field is the presence of a prominence. Another important indicator of a stressed magnetic field is the presence of sigmoid signatures discovered by Rust & Kumar (1996) and Canfield et al. (1999) with *Yohkoh*. Indeed, they have found that active regions that are sigmoidal to be the most likely to erupt. Lin (2004) pointed out that the free energy stored in a stressed magnetic structure prior to the eruption depends on the strength of the background field, so the stronger the background field, the more free energy can be stored, and thus the more energetic the eruptive process. The results obtained by Falconer et al. (2006) agree with the total nonpotentiality (total free energy) of an active region being roughly the product of the overall twist and the flux content of its magnetic field.

A positive correlation between the potential field magnetic energy of the active region and the CME speed has been found by Venkatakrishnan & Ravindra (2003). Guo et al. (2006, 2007) have found a weak correlation between the total magnetic flux of an active region and the CME speed. However, a statistical study of 49 filament eruption-associated CMEs by Chen et al. (2006) showed that the CME speeds are strongly correlated with both the average magnetic field and the total magnetic flux in the filament channel, and the corresponding linear correlation coefficients (LCCs) are 0.7 and 0.68, respectively. Using the catastrophic loss of equilibrium model, Lin (2002, 2004) found that the cases with higher background fields correspond to fast CMEs and lower fields corresponds to slow CMEs. Reeves & Forbes (2005) also found that when the background magnetic field is weak, the radiation emitted by the reconnected X-ray loops beneath a CME (i.e., flare intensity) is faint for an extended version of the Lin & Forbes (2000) model.

Good correlations have been found between different parameters representing the magnetic shear (or twist) or the nonpotentiality of the active region and the flare/CME productivity (Falconer et al. 2006; Jing et al. 2006, and references therein). As mentioned previously, several authors have found a positive correlation between the background magnetic field strength, magnetic flux, or potential magnetic field energy and the CME speed. However, to our knowledge, few studies have been made of the relationship between the magnetic shear or nonpotentiality of the background field and the intensity of flare/CME events (i.e., peak flare flux and CME speed). Our previous study (Su et al. 2007, hereafter Paper I) shows that 86% of the 50 events we examined show a strong-to-weak shear motion of the footpoints during the flare, which indicates that it is a common feature in two-ribbon flares. In Paper I, we have also measured the initial shear angle (θ_1, measured at the flare onset) and final shear angle (θ_2, measured at the time when the shear change stops) of the flare footpoints for 24 events having shear motion of the footpoints and good observations. A detailed interpretation of this shear motion is given by Su et al. (2006), according to a three-dimensional magnetic field configuration having highly sheared inner and less sheared outer magnetic field lines in the preflare

[1] Harvard-Smithsonian Center for Astrophysics, Cambridge, MA 02138.
[2] Purple Mountain Observatory, Nanjing, 210008, China; and Graduate University of Chinese Academy of Sciences, China.

phase (Moore et al. 2001, and references therein). Some detailed studies of both the shear motion and the contracting motion of the footpoints in some individual flares are carried out by Ji et al. (2006, 2007).

Solar flares can be classified as A, B, C, M, or X class according to the soft X-ray peak flux measured by *GOES*, and CME speed can also vary from less than 100 km s^{-1} to several thousand km s^{-1}. An important question is: what determines the magnitude of these quantities? In this paper we address this question by examining how the peak flare flux (PFF, Watt m^{-2}) and CME speed (V_{CME}, km s^{-1}) correlates with six magnetic parameters using a subset of two-ribbon flares selected from Paper I. Three of the parameters are measures of the magnetic size: the average background magnetic field strength (B, gauss), the area of the region where B is counted (S, cm^2), and the magnetic flux of this region (Φ, Mx). The other three parameters are measures of the magnetic shear: the initial shear angle (θ_1, degrees), the final shear angle (θ_2, degrees), and the change of shear angle ($\theta_{12} = \theta_1 - \theta_2$, degrees) of the footpoints during the flare. We examine the correlations between the intensity of flare/CME events and each of these six parameters as well as three types of multiparameter combinations. We also study the fraction of the contribution to the total variance of the observed $\log_{10}$(PFF) and V_{CME} from each parameter for these three types of combinations.

This paper is arranged as follows. The data sets and the measurement methods are described in § 2. Our results are presented in § 3, and summary and discussion are given in § 4. The detailed formulae for calculating the coronal magnetic field strength and the multiple linear regress fit are listed in the appendices.

2. DATA SELECTION AND METHODS

In Paper I, we have found that 43 out of the 50 selected two-ribbon flares show both strong-to-weak shear motion of the footpoints and ribbon separation. All of these 43 flares (which are listed in Table 1 in Paper I) have two long and parallel ribbons located on the two opposite magnetic polarities, as can be seen from a combination of the *TRACE* EUV/UV and *SOHO* MDI observations, and an example is shown in Figure 1. In this study, we first select a subset of 31 flares from the 43 flares, to examine the correlations between the $\log_{10}$(PFF), V_{CME}, and the background field strength. All of these 31 flares are associated with CMEs and have good corresponding MDI observations. Among these 31 events, 26 events are close to the disk center (longitude $< 45^\circ$), while the other 5 events are close to the solar limb (longitude $> 45^\circ$). The associated CME for each flare is identified based on both temporal (*GOES* flare peak time ± 2 hr) and spatial windows. A detailed description of the criteria can be found in Paper I. From the 31-flare sample we then select 18 flares with measured shear angles of the footpoints to examine the correlations between six magnetic parameters and the intensity of these flare/CME events.

The peak flare flux is derived from the *GOES* soft X-ray classification, which is listed in Table 1 in Paper I. In addition to the peak flare flux, we also considered the *GOES* integrated X-ray flare flux (IFF, J m^{-2}), which is taken from the National Geophysical Data Center.[3] The CME speed is the linear speed taken from the *SOHO* LASCO CME catalog.[4] Since most of our events originated near the solar disk center, they probably involve projection effect for the CME speed. In order to correct the projection effect of the CME speed, we adopt a formula by

[3] See http://www.ngdc.noaa.gov/stp/SOLAR/ftpsolarflares.html.
[4] See http://cdaw.gsfc.nasa.gov/CME_list/.

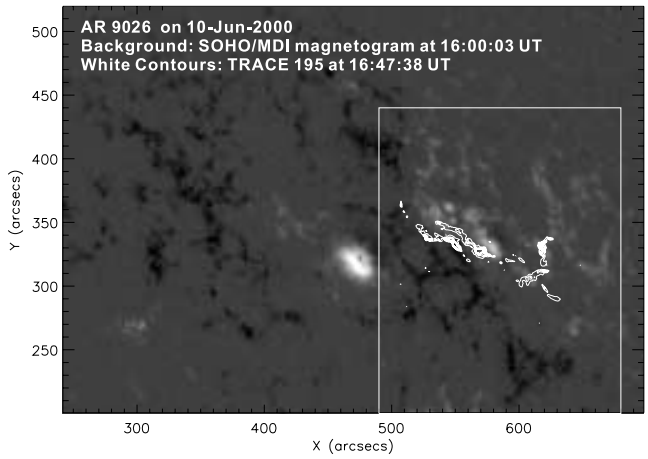

FIG. 1.—*SOHO* MDI image overlaid with *TRACE* contours (*in white*) at 195 Å on 2000 June 10. The white and black spots in MDI image show the positive and negative polarities, respectively. The area enclosed in the white box is the region where the three parameters representing the magnetic size are measured.

Leblanc et al. (2001), which assumes radial propagation of CMEs. In this formula, the radial speed (V_{rad}) is given by

$$V_{rad} = V_{sky} \frac{1 + \sin \alpha}{\sin \phi + \sin \alpha}, \quad (1)$$

in which α is the half angular width of the CME, and ϕ is the angle between the radial passing through the solar origin and the Earth direction given by $\cos \phi = \cos \lambda \cos \psi$, where λ and ψ are heliolatitude and heliolongitude, respectively. Unfortunately, it is very difficult to measure the angular width of halo CME, which is the dominating type of CMEs that we studied and also subject to projection effects. Therefore, we have taken the average angular width value (i.e., $\alpha = 36^\circ$) listed in St. Cyr et al. (2000) for all the 31 events, as suggested by Leblanc et al. (2001). Using the above formula and the coordinate information of all the events, we have estimated their radial speed as the corrected CME speed. The estimated correction factor ranges from 1.09 to 3.8. In this paper, we call the CME speed obtained directly from the catalog V_{CME}, and the radial speed after the correction of projection effect V_{C-CME}, respectively.

2.1. *Measurement Uncertainties of the Shear Angles*

Within our 31-flare sample, the shear angles (θ_1, θ_2, θ_{12}) of 20 flares have been measured and listed in Table 1 in Paper I. The shear angle is defined as the angle between the normal to the magnetic inversion line and the line connecting the conjugate footpoints. The detailed measurement method of these shear angles is illustrated in Figure 1 in Paper I. There are three types of uncertainties in the measurement of the shear angles. First, there are some uncertainties in defining conjugate footpoints, especially for the initial footpoints, which are defined as the first two brightenings that appeared at the flare onset. The difficulty arises because the corresponding postflare loops do not always show up in *TRACE* data for the initial conjugate footpoints. To minimize this uncertainty, we select 18 flares from the 20 flares having measured shear angles, because we do not see the corresponding postflare loops for the initial conjugate footpoints in the other two flares (i.e., flares on 2000 November 24 and 2003 May 31). Second, the inversion line is often difficult to define due to the separation of magnetic polarities and complex shape of the inversion line. Therefore, as described in Paper I, to measure both θ_1 and θ_2 we replaced the real complicated magnetic

inversion line with a simplified straight line, which causes some uncertainty in these two angles. However, the change of shear angle θ_{12} is unaffected by such uncertainty. Third, the footpoints always extend over multiple pixels; therefore, for each footpoint we measure an average position with some uncertainty. The uncertainty of the footpoint positions results in an uncertainty of the shear angle, which is listed in Table 1 in Paper I. Despite these uncertainties, the shear angle is a useful proxy for the nonpotential fields involved in these flares.

2.2. *Measurement Methods of the Magnetic Size*

The other three parameters (i.e., B, S, and Φ) are measured from the line of sight *SOHO* MDI magnetograms (at a cadence of 96 minutes) immediately before each flare. To measure these parameters, we first align the *TRACE* EUV/UV images with the corresponding *SOHO* MDI magnetograms. To do the alignment, we first determine the offset between the *TRACE* white light (WL) image and the corresponding MDI magnetogram. We then apply this offset to the *TRACE* EUV/UV images. Figure 1 shows a magnetogram of active region 9062 overlaid with the white contours, which refer to the two flare ribbons observed at 195 Å at 16:47:38 UT on 2000 June 10. By comparison of the MDI magnetogram with the corresponding *TRACE* EUV image, we then select a subarea (the area enclosed in the white box in Fig. 1) of the magnetogram that includes the magnetic elements immediately surrounding the flare ribbons, since these elements are expected to be the dominating magnetic fields that provide energy to the solar flares and CMEs. This selected subarea of the magnetogram is used to measure the three parameters representing the magnetic size.

MDI magnetograms systematically underestimate magnetic field strength and saturate at high magnetic field strength values (Berger & Lites 2003). Following Green et al. (2003) we first multiply the raw MDI data by 1.45 for values below 1200 G and by 1.9 for values above 1200 G to obtain the corrected flux density ($B_{\rm MDI}$). Since most of our events are not located exactly at the solar disk center, the correction for the angle between the magnetic field direction and the observer's line of sight is needed. To do this correction, we assume a purely radial magnetic field and apply the following cosine corrections to each pixel following McAteer et al. (2005):

$$B_{\rm cor} = \frac{B_{\rm MDI}}{\sin[\arccos(d/r)]}, \qquad (2)$$

where d is the distance from disk center, and r is the heliocentric radius of the solar disk, which is set to a typical value of 960″. After these corrections, we have applied two methods to measure the background magnetic field strength.

The first method (method 1) is calculating the average photospheric magnetic field strength. In each selected subarea of the magnetogram and for each magnetic polarity, we average the magnetic field strength of all pixels within a contour at 20% of the maximum magnetic field value. We select the 20% contour, because it best defines the areas of the positive and negative polarities most closely associated with the flare for our data sample. For example, if there are sunspots involved, the 20% contour will enclose the sunspots. We refer to the average magnetic field strength for the positive and negative polarities as $B_{\rm pos}$ and $B_{\rm neg}$. B is defined as the average of the absolute value of $B_{\rm pos}$ and $B_{\rm neg}$, i.e., $(|B_{\rm pos}| + |B_{\rm neg}|)/2$. The area ($S = \sum S_i$) and magnetic flux ($\Phi = \sum B_i S_i$) are the sum taken over all the pixels within this 20% contour, and B_i, S_i are the magnetic field strength and the area corresponding to each pixel, respectively. Similar to B_i, the projection effect of S_i is also corrected by applying the cosine corrections. One may argue that this method is highly arbitrary, because it depends heavily on the maximum magnetic field strength value at a single pixel. But we should note that the measurements are also controlled by the distribution of values within the 20% maximum value contour. We also tried a fixed threshold of 200 G, which includes more disconnected and weaker background fields. This method produces worse correlations with the peak flare flux and CME speed than the 20% contour method. Therefore, we will use the 20% contour method in this paper.

The second method (method 2) for measuring the background field is estimating the coronal field strength at a point P above the magnetic inversion line (MIL). The preflare magnetic field in active regions is expected to be strongly sheared, so a potential-field model cannot accurately describe the direction of the coronal field. However, to estimate the field strength, a potential-field model may be adequate. The point P is located at a height h above the photosphere. For all of the events, we set h to be 7250 km (10″), which is a typical value of the half distance between the two flare ribbons at the *GOES* flare peak time for most of the events we studied. The projection of P in the photosphere P_0 is on the magnetic inversion line (MIL) involved in the flare/CME events. The formulae we used to estimate the magnetic field strength at P are shown in Appendix A. From these formulae we find that the field strength $B_{\rm cor}$ is heavily dependent on the photospheric field at the points close to the point P_0. In order to minimize the random errors, for each event we make 10 measurements of $B_{\rm cor}$, by moving the point P_0 along the magnetic inversion line between the two flare ribbons. $B_{\rm cor}$ used below is the average of these 10 values.

3. RESULTS

3.1. *Peak Flare Flux and CME Speed versus Magnetic Field Strength*

The left four panels in Figure 2, from the top to the bottom, show scatter plots of $\log_{10}$(PFF), $\log_{10}$(IFF), $V_{\rm CME}$, and $V_{C-{\rm CME}}$ versus B (method 1) for all of the 31 events, respectively, and the right four panels show how the relationships change when B is replaced with $B_{\rm cor}$ (method 2). The solid lines show the linear fits to the data points, and the LCC of each plot is also presented in each panel.

Figure 2 shows that both B and $B_{\rm cor}$ are positively correlated with the intensity of flare/CME events represented by $\log_{10}$(PFF), $\log_{10}$(IFF), $V_{\rm CME}$, and $V_{C-{\rm CME}}$. The distribution of the points in the lower four panels of Figure 2 are more scattered and the correlations are slightly worse in comparison to the corresponding upper four panels, which may be due to larger observational uncertainties in the CME speed measurements. We also see that B has slightly worse correlations with $\log_{10}$(PFF) and $\log_{10}$(IFF), but slightly better correlations with both $V_{\rm CME}$ and $V_{C-{\rm CME}}$ than $B_{\rm cor}$. But overall, there is no significant difference between these two parameters. Therefore, we choose B to represent the background magnetic field strength in the following detailed studies.

The upper four panels of Figure 2 show that the IFF has better correlations with both B and $B_{\rm cor}$, in comparison to the PFF, but only slightly. Since there is not much difference between the scatter plots corresponding to IFF and PFF, and PFF is more widely used to represent the flare class, we choose PFF to represent the flare intensity in the following detailed study. In

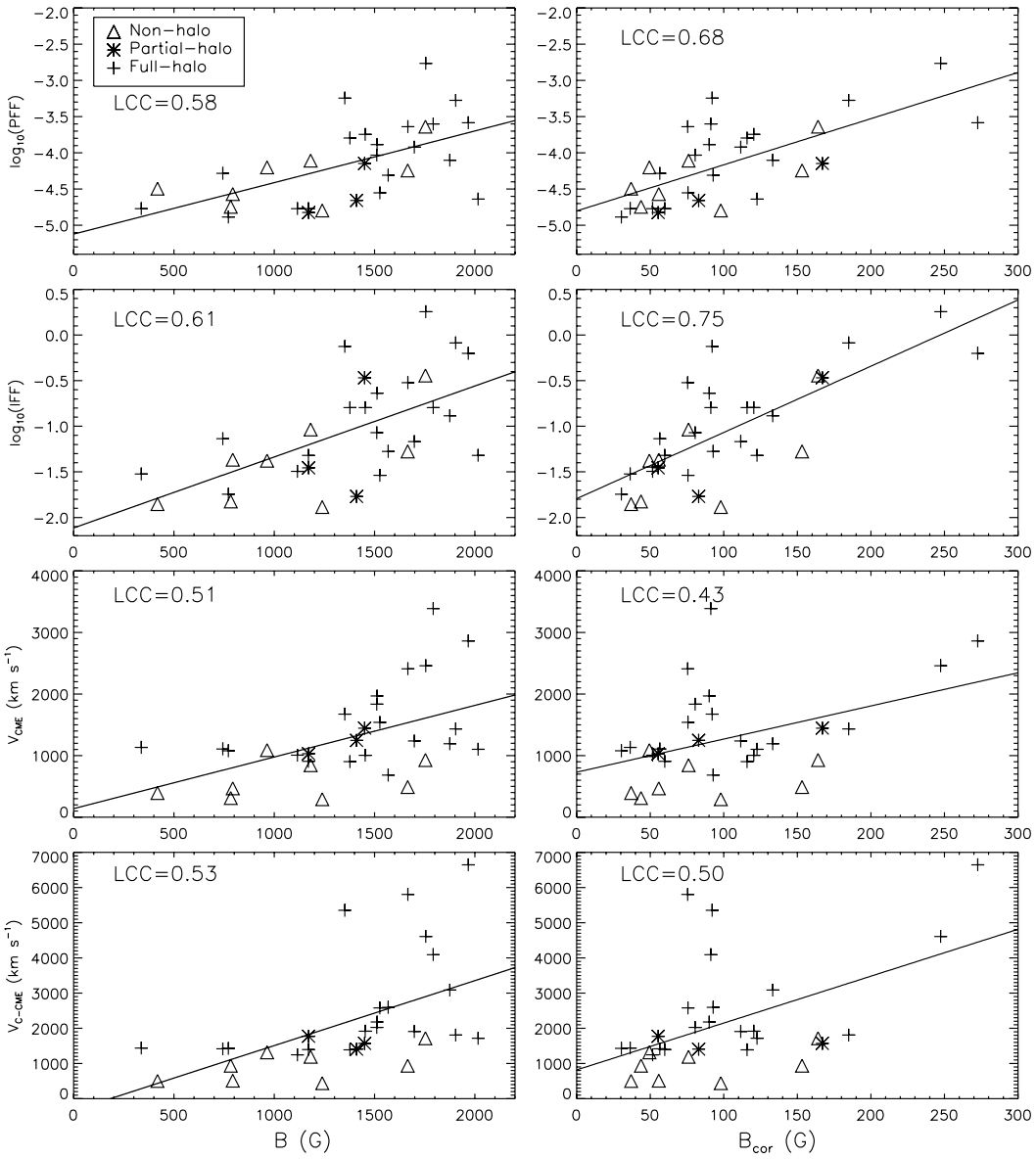

FIG. 2.—Scatter plots of the logarithm of the peak flare flux [$\log_{10}$(PFF), *top row*], the integrated flare flux [$\log_{10}$(IFF), *second row*], the CME speed ($V_{\rm CME}$, *third row*), and the corrected CME speed ($V_{C-\rm CME}$, *bottom row*) vs. the background magnetic field strength for all of the 31 events included in this paper. The magnetic field strengths in the left (B) and right ($B_{\rm cor}$) columns are calculated using methods 1 and 2, respectively. The solid lines in each panel are the linear fits to the data points, and the linear correlation coefficient (LCC) of the data points is presented in each panel. The flares associated with non-halo, partial-halo, and full-halo CMEs are marked using different symbols, i.e., triangles, asterisks, and plus signs, respectively.

comparison to $V_{\rm CME}$, the $V_{C-\rm CME}$ shows slightly better correlations with B and $B_{\rm cor}$ (see lower four panels in Fig. 2), which indicates that the correction of the CME speed has only slightly improved the correlations. Moreover, some overcorrection may exist in this correction method as suggested by Gopalswamy et al. (2001). Therefore, the original CME speed ($V_{\rm CME}$) is used to represent the CME speed in the following detailed analysis.

CMEs are categorized as non-halo, partial-halo, and full-halo CMEs for those having angular width lower than 120°, between 120° and 320°, and greater than 320°, respectively (Lara et al. 2006). The lower four panels of Figure 2 show that most of the non-halo CMEs (*triangles*) have slower speed than the partial-halo (*asterisks*) and full-halo CMEs (*plus signs*), which is consistent with the result reported by Lara et al. (2006), who propose that the observed "halo" is the manifestation (compressed material) of the shock wave driven by fast CMEs. But we do not see an obvious difference between the speeds of partial-halo and full-halo CMEs as reported by Lara et al. (2006), which may be due to our smaller data sample. We also see no obvious differences in the PFF and IFF between the flares associated with these three types of CMEs as shown in the upper four panels of Figure 2.

Figure 3*a* presents the scatter plot of the coronal field strength ($B_{\rm cor}$) versus the CME speed ($V_{\rm CME}$) for the 31 events included in this study. Different symbols represent the events with different ranges of CME mass, and those CMEs with unknown mass are marked with diamonds. The CME mass is taken from the *SOHO* LASCO CME catalog. One should note that there are generally large uncertainties in these numbers, because the estimation of the CME mass involves a number of assumptions (Vourlidas et al. 2000). Figure 3*a* shows that the CMEs with larger mass tend to have faster speed in our sample. If the magnetic forces driving the CME were roughly the same in all cases, we would expect that the CME speed is inversely related to CME mass, contrary to our finding in Figure 3*a*. This indicates

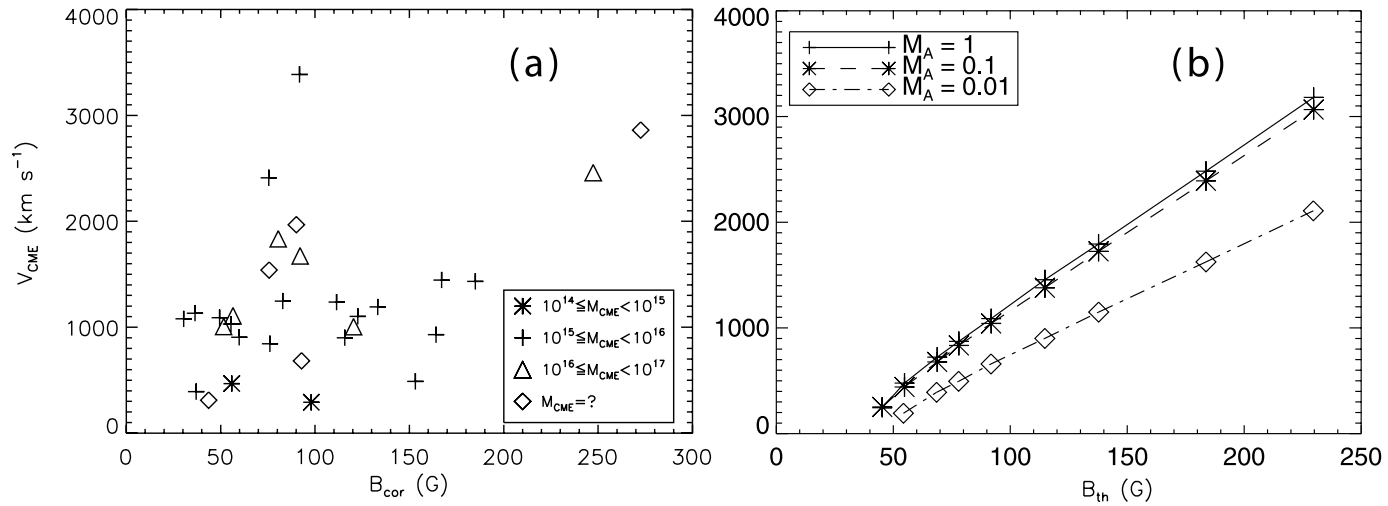

FIG. 3.—(*a*) Scatter plots of the CME speed vs. B_{cor} for all of the 31 events. B_{cor} is the magnetic field strength at a 10″ height above the photosphere, which is calculated from the observations using method 2. The CMEs with different ranges of mass (in units of g) are marked with different symbols, and those CMEs with unknown mass are marked as diamonds. (*b*) Theoretical correlation plots of CME speed and the background magnetic field strength at a 10″ height above the photosphere calculated from a catastrophic loss of equilibrium model (Reeves & Forbes 2005). The different types of lines correspond to different values of Alfvén Mach number M_A.

that the scatter in this plot is not simply due to the different CME mass.

We calculate CME speed as a function of the background field strength at 10″ height above the photosphere (B_{th}), using the extended Lin & Forbes model (2000) by Reeves & Forbes (2005). The result is shown in Figure 3*b*. The plots with different inflow Alfvén Mach number (M_A) are marked with different symbols. In the model, the CME accelerates in the early stages of the event and then asymptotically approaches a constant velocity. This constant velocity is reported in the plot and refers to a height of about three solar radii, which is similar to that of the LASCO observations. The model predicts that the CME speed increases with the background field strength, and for events with the same background field strength, the CME speed also increases with the Mach number (i.e., reconnection rate), but saturates for $M_A \geq 0.1$. This saturation occurs because the force on the flux rope due to the current sheet becomes small when $M_A \geq 0.1$ is large (see Reeves 2006). Consistent with the theoretical model, our observations show that the events with stronger background fields tend to have faster CME speeds. A comparison of Figures 3*a* and 3*b* suggests that much of the scatter in the plot of Figure 3*a* may be caused by different reconnection rates. However, there may be other contributions to the scatter in Figure 3*a*, such as the measurement uncertainties for the CME speed.

3.2. *Peak Flare Flux and CME Speed versus Six Magnetic Parameters*

In § 3.1, we examined the relationship between the intensity of the 31 flare/CME events and the background field strength. In this section, we carry out a further detailed study for a subset of 18 events with measured shear angles of the footpoints. The magnetic parameters in these 18 events we considered can be classified into two categories: parameters representing the magnetic size ($\log_{10}B$, $\log_{10}S$, and $\log_{10}\Phi$), and parameters representing the magnetic shear (θ_1, θ_2, and θ_{12}).

At first, we examine the correlations between each parameter. To do this study, we first check the correlations between the parameters in the same category. The correlation plots between each pair of parameters representing magnetic size are shown in Figures 4*a*–4*c*. We find that both $\log_{10}B$ and $\log_{10}S$ are positively correlated with $\log_{10}\Phi$. This is not surprising, because Φ is the product of B and S. We also find a weak anticorrelation between $\log_{10}B$ and $\log_{10}S$. For the other category with parameters representing magnetic shear, we find that θ_2 is highly correlated with both θ_1 and θ_{12}, as shown in Figures 4*d*–4*e*. But we find no correlation between θ_1 and θ_{12}. This result indicates that θ_2 is not an independent parameter. We then check the correlations between the parameters in different categories. We find a weak correlation between $\log_{10}B$ and θ_{12} (LCC = 0.48), while all of the other parameters in different categories are not correlated with each other (LCC $\leq$ 0.3). Figure 4*f* shows the correlation plot of θ_1 versus θ_{12}/θ_1, so it is not surprising to see a weak correlation in this plot. Figure 4*f* also shows that for the same initial shear angle, the change of shear angle can vary in a very large range in different events ($0.24 \leq \theta_{12}/\theta_1 \leq 0.96$).

For these 18 events, the correlation plots of the three parameters representing magnetic size versus $\log_{10}$(PFF) and V_{CME} are shown in the top and bottom panels of Figure 5, respectively. These parameters are $\log_{10}B$ (*left panels*), $\log_{10}S$ (*middle panels*), and $\log_{10}\Phi$ (*right panels*). Each of these three parameters is positively correlated with both $\log_{10}$(PFF) and V_{CME}. Of these parameters, $\log_{10}S$ shows relatively weak correlation with the intensity of flare/CME events, and the corresponding LCCs are 0.34. The correlation between $\log_{10}B$ and the intensity of flare/CME events appears to be slightly better but still weak (LCC*s* = 0.43, 0.38). Among these three parameters, $\log_{10}\Phi$ is the parameter that shows the best correlations with both $\log_{10}$(PFF) (LCC = 0.72) and V_{CME} (LCC = 0.62).

Similar to Figure 5, the top and bottom panels in Figure 6 show the correlation plots of the three parameters representing magnetic shear versus $\log_{10}$(PFF) and V_{CME}. These parameters are θ_1 (*left panels*), θ_2 (*middle panels*), and θ_{12} (*right panels*). θ_1 is correlated neither with $\log_{10}$(PFF) nor with V_{CME}, while θ_2 is negatively correlated with the intensity of flare/CME events (LCCs = −0.42, −0.49). θ_{12} shows good positive correlations with both $\log_{10}$(PFF) (LCC = 0.65) and V_{CME} (LCC = 0.59).

To summarize, five of these six parameters except the initial shear angle (θ_1) show either positive or negative correlations with both $\log_{10}$(PFF) and V_{CME}. Among these five parameters, the total magnetic flux of the region where the magnetic field is counted ($\log_{10}\Phi$) and the change of shear angle (θ_{12}) of the

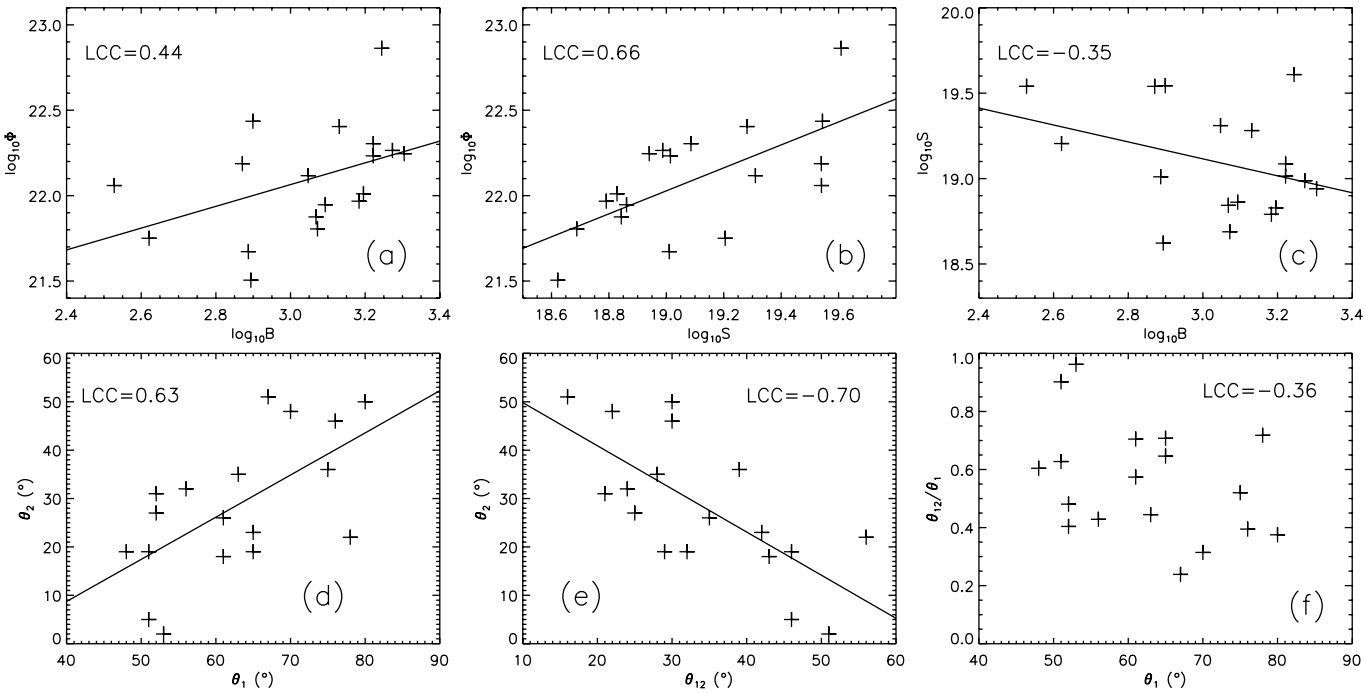

FIG. 4.—Scatter plots of six pairs of magnetic parameters measured from the 18 events with measured shear angles. (*a*) $\log_{10}B$ vs. $\log_{10}\Phi$, (*b*) $\log_{10}S$ vs. $\log_{10}\Phi$, (*c*) $\log_{10}B$ vs. $\log_{10}S$, (*d*) θ_1 vs. θ_2, (*e*) θ_{12} vs. θ_2, and (*f*) θ_1 vs. θ_{12}/θ_1. The solid lines in the figure refer to the linear fits to the data points.

footpoints during the flare are the two parameters that show the strongest correlations with the intensity of flare/CME events.

3.3. *Peak Flare Flux and CME Speed versus Multiparameter Combinations*

In § 3.2 we have found that $\log_{10}\Phi$ and θ_{12} are the two parameters that show the best correlations with the intensity of the 18 flare/CME events. One of the alternative interpretations is that Φ is a combination of B and S, while θ_{12} is a combination of θ_1 and θ_2. In the other words, only four (i.e., $\log_{10}B$, $\log_{10}S$, θ_1, and θ_2) of our six parameters are single parameter measured from observations. This result indicates that a combination of two parameters shows much better correlation with the intensity of the flare/CME events than the individual parameter. Therefore, we consider three multiparameter combinations in this section. In order to study the correlations between each of these three

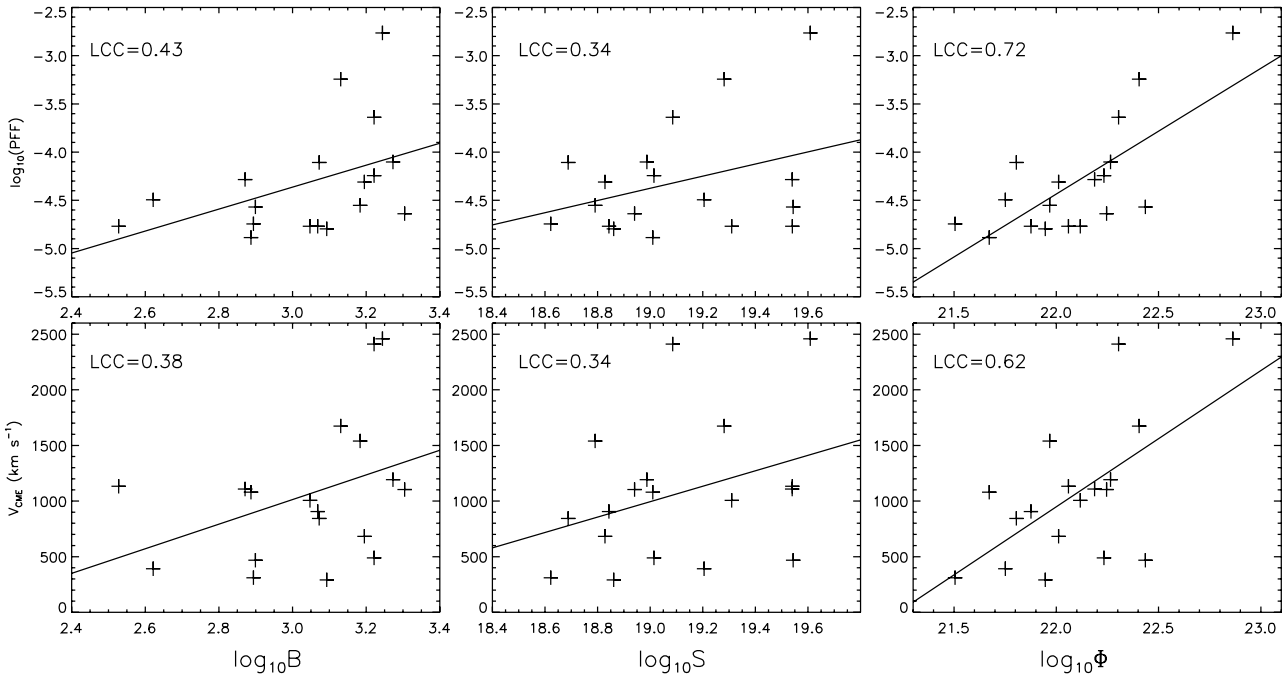

FIG. 5.—Scatter plots of $\log_{10}$(PFF) (*top panels*) and $V_{\rm CME}$ (*bottom panels*) vs. three magnetic parameters for the 18 events with measured shear angles out of our 31-event sample. The parameters, from the left to the right panels, are the logarithms of the average magnetic field strength ($\log_{10}B$), the area ($\log_{10}S$), and the magnetic flux ($\log_{10}\Phi$) of the region where B is counted, respectively. The solid lines in each figure refer to the linear fits to the data points.

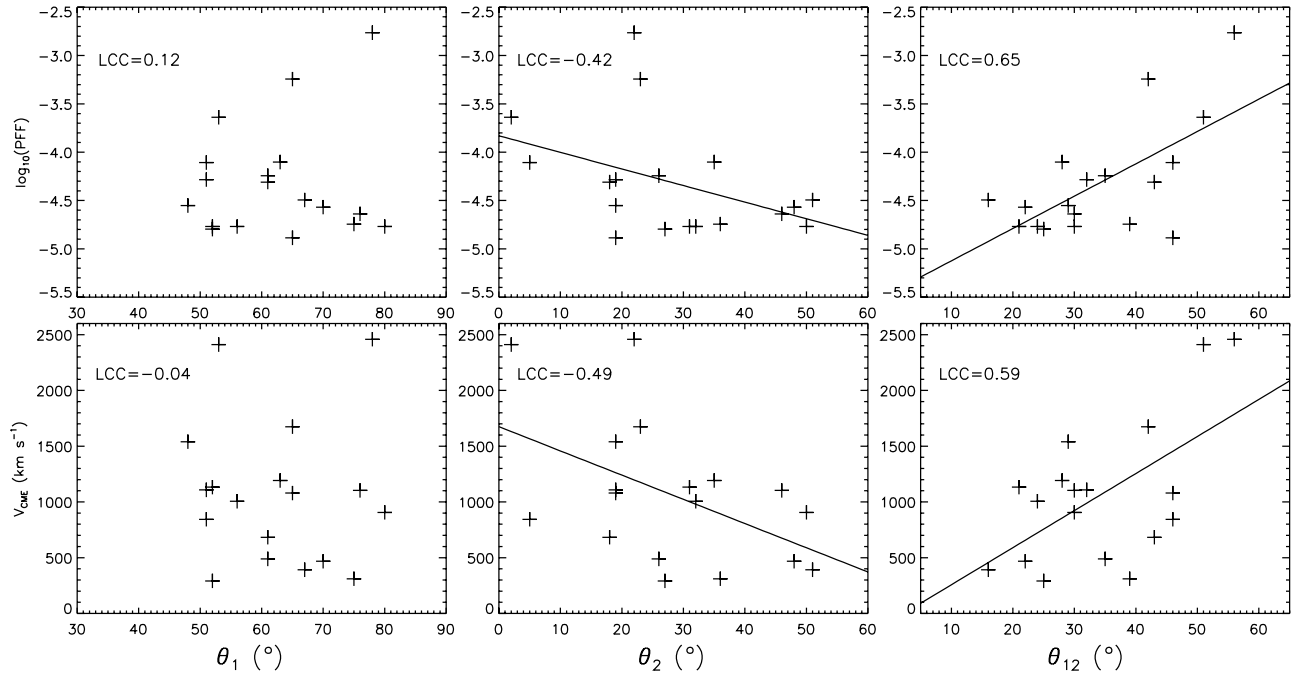

FIG. 6.—Similar to Fig. 5, but scatter plots of $\log_{10}(\mathrm{PFF})$ (*top panels*) and V_{CME} (*bottom panels*) vs. the other three parameters for the 18 events with measured shear angle. These parameters are the initial shear angle (θ_1, *left panels*), the final shear angle (θ_2, *middle panels*), and the change of shear angle (θ_{12}, *right panels*) of the footpoints, respectively.

combinations and the intensity of the flare/CME events, we have done multiple linear regression fits to the observed $\log_{10}(\mathrm{PFF})$ and V_{CME} for each combination, using the "regress" function in IDL. Appendix B shows the expression for the fitting function (Y_{fit}), which is a linear combination of all the parameters in each combination.

At first, we create a combination of four parameters (combination 1), i.e., $\log_{10}B$, $\log_{10}S$, θ_1, and θ_{12}. The first three parameters in this combination are three single parameters measured from the observations. We choose θ_{12} instead of the other single parameter θ_2 in this combination, because θ_2 appears not to be an independent parameter as shown in § 3.2. The detailed information of the fitting functions for combination 1 is listed in the left three columns of Table 1. The first column lists all the parameters in combination 1, and the constant and coefficients (as well as 1 σ uncertainty) of each parameter in the fitting functions corresponding to $\log_{10}(\mathrm{PFF})$ and V_{CME} are shown in the second and the third columns, respectively.

From the left three columns of Table 1 we can see that the coefficients of $\log_{10}B$ and $\log_{10}S$ are equal within the errors of the linear regression fit, and we also note that these two parameters may not be independent from each other (see Fig. 4*c*). Therefore, we replace $\log_{10}B$ and $\log_{10}S$ in combination 1 with a combination of them ($\log_{10}\Phi$) to create combination 2 (i.e., $\log_{10}\Phi$, θ_1, and θ_{12}). The detailed information of the fitting functions for combination 2 is listed in the middle three columns of Table 1, from which we see that the coefficient of $\log_{10}\Phi$ has smaller 1 σ uncertainty than the coefficients of both $\log_{10}B$ and $\log_{10}S$. The left panels in Figure 7, from the top to the bottom, show the scatter plots of Y_{obs} [the observed $\log_{10}(\mathrm{PFF})$ and V_{CME}] versus Y_{fit} [the fitted $\log_{10}(\mathrm{PFF})$ and V_{CME}] for combination 1; the plot for $\log_{10}(\mathrm{PFF})$ is shown in the upper left panel, and the plot for V_{CME} is shown in the lower left panel. Similar to the left panels, the middle panels in Figure 7 show the scatter plots for combinations 2. A comparison of the left and middle panels of Figure 7 shows that combination 2 has better correlation between the observed and fitted $\log_{10}(\mathrm{PFF})$ ($\mathrm{LCC} = 0.87$) than combination 1 ($\mathrm{LCC} = 0.83$). Although combination 2 has slightly worse correlation for V_{CME} ($\mathrm{LCC} = 0.79$) than combination 1 ($\mathrm{LCC} = 0.78$), overall, combination 2 appears to be better than combination 1.

The left and middle three columns of Table 1 shows that the coefficient of θ_1 are very small, and the 1 σ uncertainty in this coefficient is greater than its value. This indicates that this parameter does not play an important role in the fitting functions corresponding to both combinations 1 and 2. Therefore, we

TABLE 1

CONSTANTS, COEFFICIENTS, AS WELL AS THEIR 1 σ UNCERTAINTIES OF THE MULTIPLE LINEAR REGRESSION FITS FOR THREE TYPES OF MULTIPARAMETER COMBINATIONS

	Coefficients			Coefficients			Coefficients	
Parameter	$\log_{10}(\mathrm{PFF})$	V_{CME}	Parameter	$\log_{10}(\mathrm{PFF})$	V_{CME}	Parameter	$\log_{10}(\mathrm{PFF})$	V_{CME}
$\log_{10}B$	0.93 ± 0.49	(0.97 ± 0.60)E3	...	...	...	...	...	...
...	...	...	$\log_{10}\Phi$	1.10 ± 0.24	(1.04 ± 0.34)E3	$\log_{10}\Phi$	1.10 ± 0.23	(1.01 ± 0.34)E3
$\log_{10}S$	1.00 ± 0.30	(1.08 ± 0.37)E3	...	...	...	...	...	...
θ_1	(0.03 ± 0.87)E−2	(−0.09 ± 0.11)E2	θ_1	(−0.13 ± 0.74)E−2	(−0.10 ± 0.10)E2	...	...	...
θ_{12}	(2.86 ± 0.90)E−2	(0.29 ± 0.11)E2	θ_{12}	(2.63 ± 0.69)E−2	(0.27 ± 0.10)E2	θ_{12}	(2.62 ± 0.67)E−2	(0.27 ± 0.10)E2
Constant	−2.73E1	−2.30E4	Constant	−2.93E1	−2.23E4	Constant	−2.93E1	−2.21E4

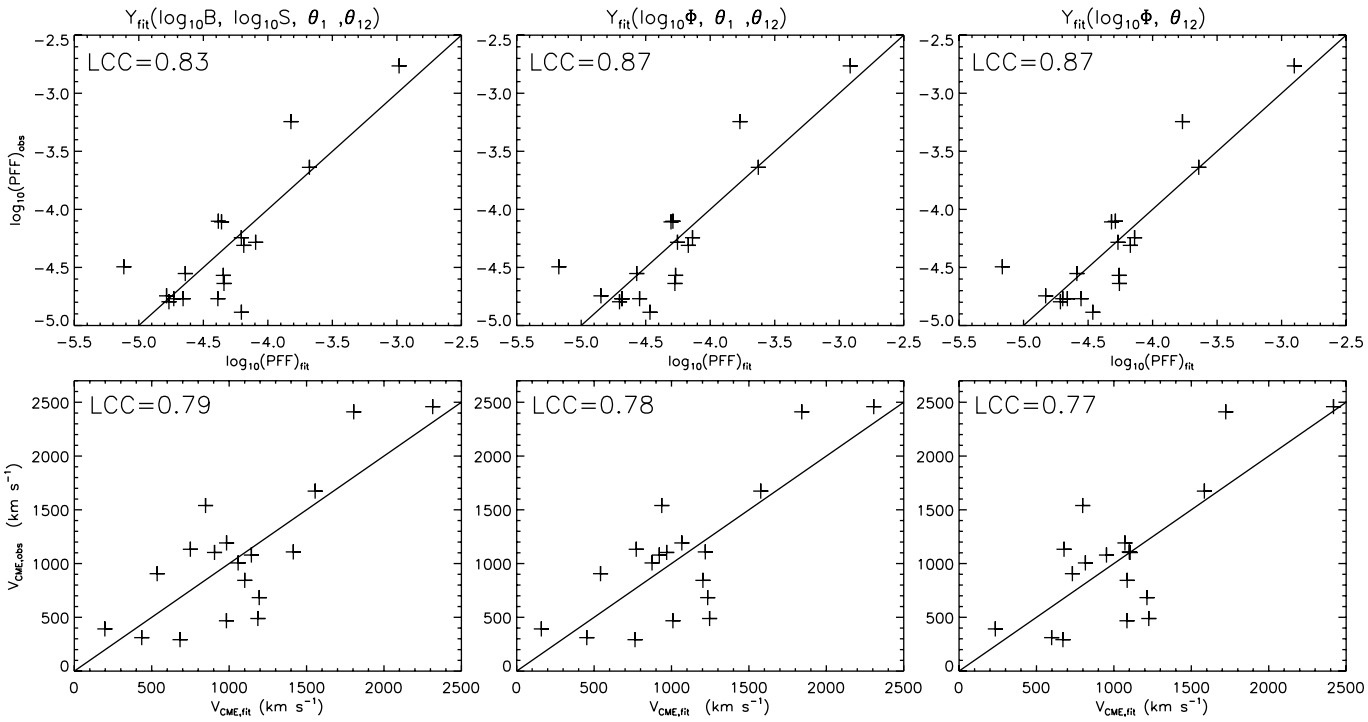

FIG. 7.—Scatter plots of the observed log 10(PFF) (*top panels*) and $V_{\rm CME}$ (*bottom panels*) vs. the fitted log 10(PFF) and $V_{\rm CME}$ ($Y_{\rm fit}$) corresponding to three types of multiparameter combinations for the 18 events with measured shear angles. *Left*: Combination 1 ($\log_{10}B$, $\log_{10}S$, θ_1, θ_{12}); *middle*: combination 2 ($\log_{10}\Phi$, θ_1, and θ_{12}); *right*: combination 3 ($\log_{10}\Phi$ and θ_{12}). The solid lines in each figure refer to the linear fits to the data points.

create combination 3 (i.e., $\log_{10}\Phi$, θ_{12}) by removing the parameter θ_1 from combination 2. The detailed information of the fitting functions for combination 3 is listed in the right three columns of Table 1. The right panels of Figure 7 show the scatter plots for combination 3, and the LCCs in these plots are only slightly worse than those in the corresponding middle panels. This further confirms that θ_1 plays only a minor role in combination 2. This result is also consistent with the fact that the coefficients and 1 σ uncertainties for $\log_{10}\Phi$ and θ_{12} in combinations 2 and 3 are very similar to each other (see Table 1).

The top panels of Figure 7 show strong and linear correlation between the observed and fitted values of $\log_{10}$(PFF) for each parameter combination, with LCCs equal or larger than 0.83. This implies that the observed magnetic parameters that we measured play an important role in determining the peak flare flux. The bottom three panels also show strong linear correlations between $V_{\rm CME}$ and the parameter combinations, but worse ($0.77 \leq$ LCC ≤ 0.79), and the distributions of the plots are more scattered than the corresponding top panels. Consistent with the earlier result found in Figure 2, this result may be caused by the larger measurement uncertainties in the CME speed as compared to the peak flare flux.

In this subsection, we have mainly addressed the question of how well the fitting function reproduces the observed intensity of flare/CME events. Now we study the contributions of the various magnetic parameters to the total variances of both $\log_{10}$(PFF) and $V_{\rm CME}$. Table 2 shows the fraction (σ_i^2) of each parameter's contribution to the total variances ($\sigma_{\rm tot}^2$) of $\log_{10}$(PFF) and $V_{\rm CME}$ for the three combinations. The calculation methods of σ_i^2 and $\sigma_{\rm tot}^2$ are presented in Appendix B. For combination 1, the largest fractional contribution to the total variances comes from $\log_{10}S$, and the second largest contribution comes from θ_{12}. The contribution from $\log_{10}B$ is slightly less than θ_{12}, while θ_1 shows significantly less contribution than the other three parameters. For both combinations 2 and 3, $\log_{10}\Phi$ is the top-ranked parameter, which shows the strongest contribution to the total variance of the intensity of flare/CME events, while θ_{12} is the second-ranked parameter. Similar to combination 1, θ_1 in combination 2 again has a very small contribution to the total variances of $\log_{10}$(PFF) and $V_{\rm CME}$. The fraction ($\sigma_o^2/\sigma_{\rm tot}^2$) of the

TABLE 2

THE CONTRIBUTIONS FROM EACH PARAMETER IN THREE TYPES OF MULTIPARAMETER COMBINATIONS (σ_i^2) AND OTHER UNKNOWN SOURCES (σ_o^2) TO THE TOTAL VARIANCES OF THE OBSERVED $\log_{10}$(PFF) ($\sigma_{\rm tot}^2 = 0.29$, PFF IS IN UNITS OF W m^{-2}) AND $V_{\rm CME}$ ($\sigma_{\rm tot}^2 = 3.45 \times 10^5$ km^2 s^{-2})

	$(\sigma_{i/o}^2/\sigma_{\rm tot}^2)100\%$			$(\sigma_{i/o}^2/\sigma_{\rm tot}^2)100\%$			$(\sigma_{i/o}^2/\sigma_{\rm tot}^2)100\%$	
PARAMETER	$\log_{10}$(PFF)	$V_{\rm CME}$	PARAMETER	$\log_{10}$(PFF)	$V_{\rm CME}$	PARAMETER	$\log_{10}$(PFF)	$V_{\rm CME}$
$\log_{10}B$	12.5%	11.2%	...	...	...	...	...	...
...	...	...	$\log_{10}\Phi$	36.7%	27.6%	$\log_{10}\Phi$	36.4%	25.7%
$\log_{10}S$	29.3%	28.3%	...	...	...	...	...	...
θ_1	0.0%	2.1%	θ_1	0.1%	2.7%	...	...	...
θ_{12}	30.7%	26.8%	θ_{12}	26.0%	23.4%	θ_{12}	25.8%	21.9%
Others	30.3%	38.1%	Others	23.5%	38.6%	Others	23.6%	41.3%

total variances due to unknown sources and/or measurement errors is also calculated and listed in Table 2 (see Appendix B for a detailed description of the method). The sum of all the fractions in each column is not 100% because of some approximations that have been made in calculating these fractions (Appendix B). For a large enough data sample, and when there is no correlation at all between magnetic parameters, this sum should be 100%. We find that the observed magnetic parameters account for a large fraction of the observed total variance; less than one-third of the variance of $\log_{10}(\mathrm{PFF})$ is due to unknown sources or measurement errors. The total variances of $\log_{10}(\mathrm{PFF})$ and V_{CME} are 0.29 (PFF is in units of W m^{-2}) and 3.45×10^5 km^2 s^{-2}, respectively.

4. SUMMARY AND DISCUSSION

For a sample of 31 two-ribbon flares associated with CMEs, we have measured the magnetic field strength (from *SOHO* MDI magnetograms) of the magnetic polarities involved in the flares using two methods: the average photospheric magnetic field strength (B) within a contour of 20% of the maximum field strength, and the magnetic field strength at a single point located at 10″ height above the photosphere (B_{cor}). We have found that both measures show that for events with larger magnetic field strength, the corresponding peak flare flux tends to be larger and the corresponding CME speed tends to be faster. This result is consistent with previous theoretical studies by Lin (2002, 2004) and Reeves & Forbes (2005), who found that the cases with higher background fields correspond to fast CMEs and strong flares, whereas lower fields correspond to slow CMEs and weak flares. This result is found through some calculations under the framework of a catastrophic loss of equilibrium model. Similar results have also been found by Chen et al. (2006) for a sample of CMEs associated solely with filament eruptions.

We have selected 18 events with measured shear angles out of the 31-event sample for further detailed study. For these 18 events, we have measured six parameters using both *SOHO* MDI magnetograms and corresponding *TRACE* observations of the flare footpoints. Three of these six parameters are measures of the magnetic size, and they are the average photospheric magnetic field strength (B), the area of the region where B is counted (S), and the magnetic flux of this region (Φ). The other three parameters represent the magnetic shear as determined from flare observations. These are the initial shear angle (θ_1, measured at the flare onset), the final shear angle (θ_2, measured at the time when the shear change stops), and the change of shear angle ($\theta_{12} = \theta_1 - \theta_2$) of the footpoints. With our six measures, we address the question what determines the intensity of the flare/CME events by examining three sets of correlations: (1) the correlations of the parameters with each other; (2) the correlations of the logarithm of the peak flare flux [$\log_{10}(\mathrm{PFF})$] as well as CME speed (V_{CME}) versus each of the six parameters; (3) the correlations of the observed $\log_{10}(\mathrm{PFF})$ and V_{CME} versus three types of multiparameter combinations, which are $\log_{10}B$, $\log_{10}S$, θ_1, and θ_{12} (combination 1); $\log_{10}\Phi$, θ_1, and θ_{12} (combination 2); and $\log_{10}\Phi$ and θ_{12} (combination 3).

The logarithms of all three parameters representing magnetic size show positive correlations with both $\log_{10}(\mathrm{PFF})$ and V_{CME}. More specifically, $\log_{10}\Phi$ shows much better correlations (LCCs = 0.72, 0.62) with both $\log_{10}(\mathrm{PFF})$ and V_{CME} than the other two parameters (LCCs $\leq$ 0.43), i.e., $\log_{10}B$ and $\log_{10}S$, probably because the magnetic flux Φ is the product of the other two parameters. This result differs from the result reported by Chen et al. (2006), who found that the average field strength is better correlated with CME speed than the magnetic flux in the filament channel for the CMEs associated with filament eruptions.

We have, for the first time, found that there are no correlations between θ_1 and $\log_{10}(\mathrm{PFF})$ as well as V_{CME}, while θ_{12} shows a strong positive correlation with the intensity of flare/CME events. The initial shear angle (θ_1) of the footpoints measured at the flare onset may represent the preflare magnetic free energy to some extent, according to our cartoon in Figure 11 in Su et al. (2006), while the change of shear angle (i.e., $\theta_{12} = \theta_1 - \theta_2$) may serve as a proxy of the released magnetic free energy during the flare, but one should keep in mind that the shear angle is not the only parameter that determines the magnetic free energy. Therefore, our result indicate that the intensity of flare/CME events may depend on the *released* magnetic free energy rather than the *total* magnetic free energy stored prior to the flare. This may make it very difficult to predict the magnitude of the flare/CME events. Emslie et al. (2004) suggested that not all of the "free" energy may be available on short timescales to power flares and CMEs, owing to the constraints imposed by helicity conservation. An alternative interpretation of the lack of correlation with θ_1 is that this result is due to the large uncertainties in our measurements of the shear angles, which are fully discussed in § 2.1. More specifically, the uncertainty in the definition of magnetic inversion line may cause large uncertainties in measuring both θ_1 and θ_2, while the change of shear angle is unaffected by such uncertainty. The fact that for the same initial shear angle (θ_1), the change of shear angle (θ_{12}) can vary greatly in different events (Fig. 4*f*) may indicate that the released free magnetic energy could be different in the active regions with the same stored total free energy prior to the eruptions.

For each of the three types of multiparameter combinations we have done multiple linear regression fits to the observed $\log_{10}(\mathrm{PFF})$ and V_{CME}. For each combination the corresponding fitting functions are a linear combination of all the parameters in this combination. We have also calculated the fraction of each parameter's contribution to the total variances of $\log_{10}(\mathrm{PFF})$ and V_{CME}. For all of the three combinations, we see strong linear correlations between the observed and fitted values of $\log_{10}(\mathrm{PFF})$ and V_{CME}. This implies that the observed magnetic parameters play an important role in determining the intensity of the flare/CME events. Furthermore, all three combinations show better correlation with the intensity of flare/CME events than any individual magnetic parameter. Among these three combinations, combination 2 ($\log_{10}\Phi$, θ_1, and θ_{12}) shows the strongest linear correlation between the observed and fitted values of both $\log_{10}(\mathrm{PFF})$ and V_{CME}. This result indicates that it is very useful to combine B and S into a single magnetic parameter, the flux Φ. Combination 3 ($\log_{10}\Phi$ and θ_{12}) shows only slightly worse correlation with the intensity of flare/CME events than combination 2. Moreover, in combination 2, the fractions of the contribution to the total variances of $\log_{10}(\mathrm{PFF})$ and V_{CME} from both $\log_{10}\Phi$ (36.7% and 27.6%) and θ_{12} (26.0% and 23.4%) are significantly greater than θ_1 (0.1% and 2.7%). These results imply that the initial shear angle θ_1 only plays a minor role in determining the peak flare flux and CME speed, which is consistent with the result reported in the last paragraph. These results also suggest that the magnetic flux of the region, where the magnetic field is counted (Φ), and the change of shear angle of the footpoints during the flare (θ_{12}) are two separate but comparably important parameters in determining the intensity of flare/CME events. In other words, large released free energy (a combination of Φ and θ_{12}) tends to produce large flares and fast CMEs.

Although the fitting functions corresponding to the three multiparameter combinations show very strong and linear correlations with the intensity of flare/CME events, we still can see some scatter in these plots (Fig. 7). Some of this scatter may result from different reconnection rates, different durations of reconnection and CME acceleration, different configurations of the ambient magnetic field, and measurement uncertainties. First of all, as shown in Figure 3*b* different reconnection rates may cause the scatter of CME speed, if the background field strength is fixed. Accordingly, different reconnection rates may also cause the scatter of the peak flare flux, if the other parameters are fixed. This is because the fraction of the released energy that is converted into flare or CME energy depends on the reconnection rate as reported by Reeves & Forbes (2005), who also found that greater than 50% of the released energy becomes flare energy when $M_A < 0.006$. Secondly, although many events with larger CME speed and greater peak flare flux tend to originate from strong magnetic field regions, the weak magnetic fields could also produce large CME speed if the durations of reconnection and acceleration are very long as illustrated in Qiu & Yurchyshyn (2005). Thirdly, Liu (2007) found that CMEs under heliospheric current sheet are significantly slower than CMEs under unidirectional open field structures. This implies that the ambient magnetic field structure plays a role in determining the speed of halo CMEs. Therefore, different ambient magnetic structure may make some contributions to the scatter of the plots in the bottom panels of Figure 7. Finally, many uncertainties existed in our measurements of the six parameters and the measurements of CME speed. This may also add some contributions to the scatter of the plots in Figure 7.

In summary, the magnetic flux (Φ) and the change of shear angle (θ_{12}) of the footpoints during the flare show the most significant correlations with the intensity of flare/CME events [$\log_{10}$(PFF), V_{CME}]. The fact that both $\log_{10}$(PFF) and V_{CME} are highly correlated with the change of shear angle (θ_{12}) rather than with the initial shear angle (θ_1) indicates that the intensity of flare/CME events may depend on the *released* magnetic free energy rather than the *total* free energy stored prior to the flare. We also found that a linear combination of a subset of our six parameters shows a much better correlation with the intensity of flare/CME events than each parameter itself, and the combination of $\log_{10}\Phi$, θ_1, and θ_{12} is the top-ranked combination. Moreover, in this combination, the fractions of the contribution to the total variances of $\log_{10}$(PFF) and V_{CME} from both $\log_{10}\Phi$ and θ_{12} are significantly greater than θ_1.

We sincerely thank the anonymous referee for constructive suggestions which have been very useful in improving this paper. Y. N. Su is grateful to Jun Lin, Steven Saar, Guangli Huang, and Monica Bobra for helpful discussions and suggestions. The authors wish to thank the teams of *TRACE*, *SOHO* MDI, and *SOHO* LASCO for providing the valuable data. The CME Catalog (see footnote 4) is generated and maintained at the CDAW Data Center by NASA and The Catholic University of America in cooperation with the Naval Research Laboratory. *SOHO* is a project of international cooperation between ESA and NASA. The *TRACE* analysis was supported at Smithsonian Astrophysics Observatory (SAO) by a contract from Lockheed Martin. Y. N. Su was supported by an SAO Predoctoral Fellowship, the NSFC projects with grants 10333030 and 10273025, and "973" program with grant 2006CB806302.

APPENDIX A

ESTIMATE OF THE CORONAL MAGNETIC FIELD STRENGTH

To estimate the coronal magnetic field strength in the flaring active region, we use a simple potential-field model. Let P be a point at height h above the magnetic inversion line and let P_0 be the projection of P on the photosphere. We use a Cartesian coordinate system (x, y, z) with the origin at P_0; x and y are the horizontal coordinates along and perpendicular to the magnetic inversion line, respectively, and z is the height above the photosphere. The point P is located at $r = (0, 0, h)$, and the potential field $B_{cor}(r)$ at this point can be estimated using the formula

$$B_{cor}(r) = \int\int \frac{B_0(x_0, y_0)(r - r_0)}{2\pi|r - r_0|^3}\, dx_0\, dy_0, \tag{A1}$$

where $B_0(x_0, y_0)$ is the photospheric radial field strength at point $r = (x_0, y_0, 0)$ in the selected subarea of the magnetogram. Equation (A1) can be written as

$$\begin{aligned} B_{cor,x} &= -\sum_{ij} \frac{B_{0,ij} x_{0,i}}{2\pi(x_{0,i}^2 + y_{0,j}^2 + h^2)^{3/2}}, \\ B_{cor,y} &= -\sum_{ij} \frac{B_{0,ij} y_{0,j}}{2\pi(x_{0,i}^2 + y_{0,j}^2 + h^2)^{3/2}}, \\ B_{cor,z} &= \sum_{ij} \frac{B_{0,ij} h}{2\pi(x_{0,i}^2 + y_{0,j}^2 + h^2)^{3/2}}, \end{aligned} \tag{A2}$$

and the field strength of the potential field is

$$B_{cor} = |B_{cor}(r)| = \sqrt{B_{cor,x}^2 + B_{cor,y}^2 + B_{cor,z}^2}. \tag{A3}$$

The height of h of point P is assumed to be 7250 km (10″). In this method, all points in the selected subarea of the magnetogram contribute to the coronal field strength at point P.

APPENDIX B

MULTIPLE LINEAR REGRESSION FIT

To study the relationship between the observed $\log_{10}(\mathrm{PFF})$ as well as V_{CME} and the observed magnetic parameters (i.e., $\log_{10}B$, $\log_{10}S$, $\log_{10}\Phi$, θ_1, and θ_{12}) for our 18-event sample, we perform a multiple linear regression fit to the observed data by fitting a general linear equation. The fitting equation is expressed as

$$Y_{\mathrm{fit},j} = a_0 + \sum_{i=1}^{m} a_i X_{ij}, \tag{B1}$$

where X_{ij} is the measurement of the magnetic parameter i (e.g., $\log_{10}B_i$ or $\theta_{12,j}$, where $j = 1, 2, \ldots n$); and $Y_{\mathrm{fit},j}$ refers to the fitted values of $\log_{10}(\mathrm{PFF})$ and V_{CME}. In this equation, a_0 is a constant, a_i is the coefficient of each magnetic parameter, m is the number of parameters used in the fit, and n is the flare events number. Let $Y_{\mathrm{obs},j}$ be the observed values of $\log_{10}(\mathrm{PFF})$ and V_{CME}. The mean value of $Y_{\mathrm{fit},j}$ is assumed to be equal to the mean value of $Y_{\mathrm{obs},j}$, so equation (B1) yields

$$Y_{\mathrm{fit},j} - \overline{Y_{\mathrm{obs}}} = \sum_{i=1}^{m} a_i\left(X_{ij} - \overline{X_i}\right), \tag{B2}$$

where $\overline{X_i}$ is the mean value of parameter X_{ij}.

The variance of $Y_{\mathrm{obs},j}$ due to a known magnetic parameter X_{ij} is defined as

$$\sigma_i^2 = \frac{1}{n}\sum_{j=1}^{n}\left[a_i(X_{ij} - \overline{X_i})\right]^2, \tag{B3}$$

and the variance due to other unknown parameters and/or measurement errors is defined as

$$\sigma_o^2 = \frac{1}{n}\sum_{j=1}^{n}(Y_{\mathrm{obs},j} - Y_{\mathrm{fit},j})^2. \tag{B4}$$

The total variance of $Y_{\mathrm{obs},j}$ is

$$\begin{aligned}\sigma_{\mathrm{tot}}^2 &= \frac{1}{n}\sum_{j=1}^{n}\left(Y_{\mathrm{obs},j} - \overline{Y_{\mathrm{obs}}}\right)^2 = \frac{1}{n}\sum_{j=1}^{n}\left[(Y_{\mathrm{obs},j} - Y_{\mathrm{fit},j}) + (Y_{\mathrm{fit},j} - \overline{Y_{\mathrm{obs}}})\right]^2 \\ &= \frac{1}{n}\sum_{j=1}^{n}\left[\left(Y_{\mathrm{obs},j} - Y_{\mathrm{fit},j}\right)^2 + 2(Y_{\mathrm{obs},j} - Y_{\mathrm{fit},j})(Y_{\mathrm{fit},j} - \overline{Y_{\mathrm{obs}}}) + (Y_{\mathrm{fit},j} - \overline{Y_{\mathrm{obs}}})^2\right].\end{aligned} \tag{B5}$$

The last term on the right-hand side of equation (B5) can be written as

$$\frac{1}{n}\sum_{j=1}^{n}(Y_{\mathrm{fit},j} - \overline{Y_{\mathrm{obs}}})^2 = \frac{1}{n}\sum_{j=1}^{n}\left[\sum_{i=1}^{m} a_i(X_{ij} - \overline{X_i})\right]^2 = \frac{1}{n}\sum_{j=1}^{n}\left\{\sum_{i=1}^{m}\left[a_i(X_{ij} - \overline{X_i})\right]^2 + 2\sum_{k\neq i} a_i a_k (X_{ij} - \overline{X_i})(X_{kj} - \overline{X_j})\right\} \tag{B6}$$

The second terms on the right-hand side of equations (B5) and (B6) will be very small and can be neglected if there are no correlations between different magnetic parameters, and the sample is big enough. After inserting equations (B3) and (B4) to equation (B5), the total variance of $Y_{\mathrm{obs},j}$ can be approximated as

$$\sigma_{\mathrm{tot}}^2 \approx \sigma_o^2 + \sum_{i=1}^{m}\sigma_i^2. \tag{B7}$$

REFERENCES

Berger, T., & Lites, B. W. 2003, Sol. Phys., 213, 213
Canfield, R. C., Hudson, H. S., & McKenzie, D. E. 1999, Geophys. Res. Lett., 26, 627
Chen, A. Q., Chen, P. F., & Fang, C. 2006, A&A, 456, 1153
Emslie, A. G., et al. 2004, J. Geophys. Res., 109, A10104
Falconer, D. A., Moore, R. L., & Gary, G. A. 2006, ApJ, 644, 1258
Gopalswamy, N., Yashiro, S., Kaiser, M. L., Howard, R. A., & Bougeret, J.-L. 2001, J. Geophys. Res., 106, 29219
Green, L. M., Démoulin, P., Mandrini, C. H., & Van Driel-Gesztelyi, L. 2003, Sol. Phys., 215, 307
Guo, J., Zhang, H. Q., & Chumak, O. V. 2007, A&A, 462, 1121
Guo, J., Zhang, H. Q., Chumak, O. V., & Liu, Y. 2006, Sol. Phys., 237, 25

Ji, H. S., Huang, G. L., & Wang, H. M. 2007, ApJ, 660, 893
Ji, H. S., Huang, G. L., Wang, H. M., Zhou, T. H., Li, Y. P., Zhang, Y. A., & Song, M. T. 2006, ApJ, 636, L173
Jing, J., Song, H., Abramenko, V., Tan, C. Y., & Wang, H. M. 2006, ApJ, 644, 1273
Lara, A., Gopalswamy, N., Xie, H., Mendoza-Torres, E., Pérez-Eríquez, & Michalek, G. 2006, J. Geophys. Res., 111, A06107
Leblanc, Y., Dulk, G. A., Vourlidas, A., & Bourgeret, J. L. 2001, J. Geophys. Res., 106, 25301
Lin, J. 2002, Chinese J. Astron. Astrophys., 2, 539
———. 2004, Sol. Phys., 219, 169
Lin, J., & Forbes, T. 2000, J. Geophys. Res., 105, 2375
Liu, Y. 2007, ApJ, 654, L171
McAteer, R. T. J., Gallagher, P. T., Ireland, J., & Young, C. A. 2005, Sol. Phys., 228, 55
Moore, R. L., Sterling, A. C., Hudson, H. S., & Lemen, J. R. 2001, ApJ, 552, 833
Priest, E. R., & Forbes, T. G. 2002, Astron. Astrophys. Rev., 10, 313
Qiu, J., & Yurchyshyn, V. B. 2005, ApJ, 634, L121
Reeves, K. K. 2006, ApJ, 644, 592
Reeves, K. K., & Forbes, T. G. 2005, ApJ, 630, 1133
Rust, D. M., & Kumar, A. 1996, ApJ, 464, L199
St. Cyr, O. C., et al. 2000, J. Geophys. Res., 105, 18169
Su, Y. N., Golub, L., & Van Ballegooijen, A. A. 2007, ApJ, 655, 606 (Paper I)
Su, Y. N., Golub, L., Van Ballegooijen, A. A., & Gros, M. 2006, Sol. Phys., 236, 325
Venkatakrishnan, P., & Ravindra, B. 2003, Geophys. Res. Lett., 30, 2181
Vourlidas, A., Subramanian, P., Dere, K. P., & Howard, R. A. 2000, ApJ, 534, 456